RSC Advances

PAPER

View Article Online
View Journal | View Issue

Check for updates

Cite this: *RSC Adv.*, 2017, 7, 32442

Three-dimensional architecture of Ag/CeO$_2$ nanorod composites prepared by dealloying and their electrocatalytic performance†

Xiaolong Zhang,[ab] Guijing Li,[b] Xiaoping Song,[a] Sen Yang *[a] and Zhanbo Sun *[a]

Received 25th April 2017
Accepted 19th June 2017

DOI: 10.1039/c7ra04651k

rsc.li/rsc-advances

A novel three-dimensional (3D) architecture of Ag/CeO$_2$ nanorods with high electrocatalytic activity was prepared by dealloying melt-spun Al–Ag–Ce alloys in NaOH aqueous solutions for NaBH$_4$ electro-oxidation. The nanorod composite was composed of CeO$_2$ nanorods and large-size Ag nanoparticles. After undergoing calcination at 573 K in air, many highly dispersed small Ag nanoparticles were generated and deposited on the surface of the CeO$_2$ nanorod framework. Well-defined Ag/CeO$_2$ interfaces were created *via* the anchoring of small Ag nanoparticles on the CeO$_2$ nanorods, and the nanorods were connected by larger conductive Ag nanoparticles. Electrochemical measurements showed that the mass specific current of the Ag/CeO$_2$ composites was 2.5 times higher than that of pure Ag for BH$_4^-$ oxidation. The Ag/CeO$_2$ composites exhibited enhanced catalytic activity owing to the 3D nanorod architecture, strong interfacial interactions between small Ag nanoparticles and CeO$_2$ nanorods, and high concentrations of surface oxygen species.

1. Introduction

The direct borohydride fuel cell (DBFC) is considered a promising power source for the direct conversion of chemical fuels to electricity due to its high specific capacity and cell voltage.[1–4] The electrocatalytic oxidation of borohydride is a crucial reaction at DBFC anodes. Noble metal-based nanostructured anode electrocatalysts, such as Pt, Pd and Au, have exhibited high catalytic activities for the electro-oxidation of borohydride.[1,2,4–6] However, the high cost and low reserves of noble metals have restricted their application, and thus have stimulated extensive studies to develop low-cost electrocatalysts with high efficiencies. To efficiently utilize noble metals, one can tune their structures to control particle size or combine them with metal oxides to form composites.[7,8] The construction of a 3D noble metal/oxide architecture could take full advantage of optimized structures and maximize metal/oxide interface area.[9–11]

Ceria (CeO$_2$) is known to be an excellent additive to promote various catalytic reactions because of its ability to store and release oxygen with a reversible Ce^{4+}/Ce^{3+} transition, high oxygen carrying capacity and lower price.[12–16] CeO$_2$/noble metal composites can often give rise to significant improvements in their activities due to the synergistic interface interaction between them, which are widely exploited in the field of fuel cells,[17,18] methane oxidation,[19] CO oxidation[11,20] *etc.* Among noble metals, Ag is less expensive and more abundant than other noble metals. Ag–CeO$_2$ composites have been demonstrated to be very competent at catalyzing many important oxidation reactions.[21–25] However, Ag nanoparticles wrapped by a CeO$_2$ shell might not be suitable for electrocatalytic applications due to the low electron conductivity of CeO$_2$. Consequently, it is necessary to enhance the structural design of catalysts in order to reduce the negative effects associated with low electron conductivity and the lack of attachment between Ag and CeO$_2$. To improve the conductivities of CeO$_2$-containing catalysts, several strategies that focus on the optimization of morphologies or structures have been adopted, one of which involves supporting the catalysts on electrically conductive materials such as carbon, carbon nanotubes, or graphene.[14,17,18,26] However, the many synthetic steps, high calcination temperatures and harsh conditions of the process are difficult to handle.

Recently, dealloying has been recognized as an effective method for the fabrication of nanoporous noble metals and their alloys, which have good conductivities.[27,28] In our previous work, we designed a novel nanoporous Ag@CeO$_2$ structure in which CeO$_2$ nanoparticles were loaded on the surface of Ag ligaments *via* dealloying, and their electrocatalytic activity was effectively enhanced.[29] There was only a small amount of CeO$_2$ added in the composite, which still requires a considerable

---

[a] *School of Science, MOE Key Laboratory for Non-Equilibrium Synthesis and Modulation of Condensed Matter, Key Laboratory of Shaanxi for Advanced Functional Materials and Mesoscopic Physics, State Key Laboratory for Mechanical Behavior of Materials, Xi'an Jiaotong University, Xi'an 710049, P. R. China. E-mail: szb@mail.xjtu.edu.cn; yangsen@mail.xjtu.edu.cn; Fax: +86 29 82665995; Tel: +86 29 82665995*

[b] *Department of Engineering Mechanics, Shijiazhuang Tiedao University, Shijiazhuang 050043, P. R. China*

† Electronic supplementary information (ESI) available. See DOI: 10.1039/c7ra04651k

amount of Ag as the conductive material. In addition, annealing temperature and time also strongly influence on the performance of the hybrid Ag-containing nanocomposites.[29–31] Therefore, it is of great importance to fully utilize noble metal/oxide interfaces to generate stable Ag/CeO_2 electrocatalysts with low Ag contents and high performances.

In this work, we fabricated well-defined Ag/CeO_2 interface nanostructures and assembled a monolithic Ag/CeO_2 composite for electrocatalysis *via* a facile dealloying method. A 3D Ag/CeO_2 architecture composed of CeO_2 nanorods as the framework and Ag particles connecting them was directly constructed by dealloyed Al–Ce–Ag precursor alloys. After calcination, the ultrasmall Ag nanoparticles were loaded *in situ* on the CeO_2 architecture, resulting in the formation of bimodal Ag. The electrocatalytic performance of this 3D Ag/CeO_2 architecture was investigated and exhibited an enhanced activity and good stability for the electrooxidation of sodium borohydride. The formation mechanism of this unique structure was also discussed.

2. Experimental

2.1 Preparation of the Ag/CeO_2 nanorod architecture

Al–Ag–Ce alloys with nominal compositions of $Al_{81}Ag_{15}Ce_4$, $Al_{79}Ag_{15}Ce_6$, $Al_{84}Ag_{10}Ce_6$, $Al_{85}Ag_{15}$ and $Al_{90}Ce_{10}$ alloys were prepared from pure Al (99.90 wt%), pure Ag (99.99 wt%) and pure Ce (99.90 wt%) by arc-melting using high-purity Ar as the protective atmosphere. Subsequently, the pre-alloyed ingots were re-melted in a quartz tube and heated by high frequency induction melting. Then, the metal solution was blown onto the surface of a single roller melt spinning at the speed of 33 m s^{-1}. The melt-spun resulting ribbons were typically 20–60 μm in thickness and 2–4 mm in width.

The melt-spun ribbons were dealloyed in a 5 wt% NaOH aqueous solution at 333 K for 12 h. The as-dealloyed samples were rinsed several times with reverse osmosis water and then with dehydrated alcohol. Subsequently, the dealloyed Al–Ag–Ce and $Al_{90}Ce_{10}$ ribbons were calcined at 573 K for 2 h (hereafter, Al–Ag–Ce ribbons-573 K).

2.2 Characterization methods

The phase constitutions of the prepared samples were analyzed using a Bruker D8 Advance X-ray diffractometer (XRD). The semiquantitative analysis for the dealloyed Al–Ag–Ce ribbons-573 K was carried out by Jade 6.5 software using reference intensity ratio (RIR) method from the ratio of XRD peak integrated intensity (peak area). The chemical analysis was determined by X-ray fluorescence spectrometry (XRF) using an S8 Tiger Bruker spectrometer. The microstructures and compositions were characterized using a JEM-2100 high-resolution Transmission Electron Microscope (TEM) and a JSM-7000F field emission Scanning Electron Microscope (SEM) equipped with an INCA X-Sight Oxford Energy Dispersive X-ray Spectrometer (EDX). All the SEM photos were acquired in the secondary electron imaging (SEI) mode. The compositions of the samples were determined by EDX.

X-ray photoelectron spectroscopy (XPS) studies were performed using an Axis Ultra Kratos (UK) multifunctional spectrometer using monochromatic Al Kα radiation. Smoothing, background removal and peak fitting were carried out with a CasaXPS analysis software. N_2 adsorption measurements were performed on a Micromeritics ASAP 2020 instrument at −77 K, and the samples were outgassed for 2 h in vacuum on the degassing port of the analyzer at 523 K prior to the Brunauer–Emmett–Teller (BET) surface area measurement. The surface areas of the samples were determined by the BET method, and the pore size distribution was determined by the desorption branch of the isotherm using the Barrett–Joyner–Halenda (BJH) algorithm.

2.3 Electrochemical measurements

Electrochemical measurements were performed on a Versa STAT MC workstation in a standard three-electrode cell with a Pt net serving as the counter electrode and a saturated Ag/AgCl, KCl electrode used as the reference. The working electrodes were prepared as follows: 5.0 mg of the as-prepared composite, 1.0 mg of acetylene black, 200.0 μL of isopropanol, and 200.0 μL of Nafion solution (DuPont: 0.5 wt%) were ultrasonically mixed. Four microliters (μL) of the catalyst ink was placed on a polished 3 mm diameter glassy carbon working electrode. The performances of the catalysts towards $NaBH_4$ electro-oxidation was evaluated by cyclic voltammetry (CV) and chronoamperometric (CA) curves, which were collected in 0.5 M KOH + 0.01 M $NaBH_4$ solution at room temperature under the protection of high-purity N_2. The 0.5 M KOH electrolyte was deaerated with high purity nitrogen for thirty minutes before the electrochemical measurements. The current density was normalized by the geometric area of the glassy carbon working electrode and by the mass of Ag. The catalytic performance of the nanoporous Ag without CeO_2 prepared from dealloyed $Al_{85}Ag_{15}$ alloy was also carried out under the same experimental conditions. Electrochemical impedance spectroscopy (EIS) was obtained in the frequency range of 1000 kHz to 1 Hz at −0.8 V using a CHI-660E electrochemical workstation (Shanghai, China). The results were represented in Nyquist plots.

3. Results and discussion

3.1 Microstructure of the Ag/CeO_2 nanorod architecture

Fig. 1 shows the XRD patterns of precursor alloys before and after dealloying, and the dealloyed ribbons calcined in air. The as-quenched alloy ribbons, as shown in Fig. 1a, consisted of an α-Al (Ag, Ce) solid solution, $Ag_{7.32}Al_{9.86}Ce_{1.61}$ and an unidentified Al–Ce intermetallic compound (denoted Al_xCe_y). After the ribbons were dealloyed, the diffraction peaks of the α-Al, Al_xCe_y and $Ag_{7.32}Al_{9.86}Ce_{1.61}$ intermetallic compounds disappeared, and only that of fcc-Ag could be detected (Fig. 1b). This result suggests that the precursor alloys are decomposed during dealloying. The diffraction peaks related to Ce could not be detected in the as-dealloyed ribbons. However, when the dealloyed samples were calcined at 573 K, the diffraction peak of

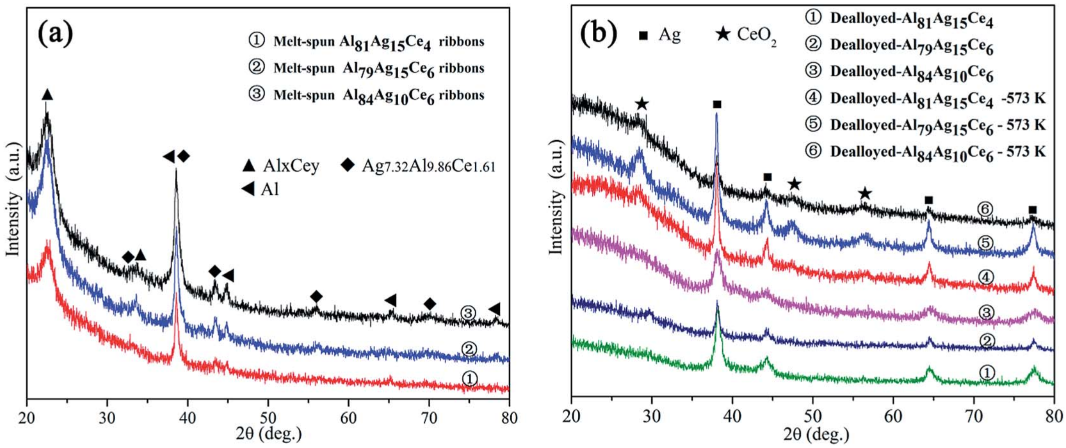

Fig. 1 XRD patterns of the melt-spun Al–Ag–Ce ribbons before and after dealloying and the dealloyed ribbons calcined at 573 K.

CeO_2 could be detected, indicating that Ce existed in another form for the as-dealloyed samples.

The relative amounts of Ag and CeO_2 in the Ag/CeO_2 composites were determined from XRD data (Fig. S1†) using RIR analysis and the results are shown in Table S1.† The chemical composition of the Ag/CeO_2 samples by XRF is also presented in Table S1.† The amount of CeO_2 in the calcined samples increased with increasing Ce content in the precursor alloys. The EDX results of the melt-spun Al–Ag–Ce ribbons and the dealloyed ribbons-573 K are provided in Table S2.† The results of the melt-spun Al–Ag–Ce ribbons indicated that the ribbons contained Al, Ag and Ce, with a near nominal composition. According to the Ag/Ce ratio for the dealloyed ribbons-573 K, the nominal Ag amounts (wt%) in Ag/CeO_2 prepared from the dealloyed $Al_{81}Ag_{15}Ce_4$, $Al_{79}Ag_{15}Ce_6$, and $Al_{84}Ag_{10}Ce_6$ ribbons-573 K were 70.68%, 59.58%, and 49.73%, respectively; all of which were close to their actual contents as confirmed by XRF. The results demonstrated that the Ag/Ce atomic and weight ratios were in good agreement with those of the precursor alloys.

Fig. 2 shows the microstructures of the dealloyed Al–Ag–Ce samples-573 K. The surfaces of the dealloyed Al–Ag–Ce samples-573 K exhibited a nanocomposite structure composed of a nanoporous matrix and with a needle-like a phase morphology embedded in the matrix. The average particle size was approximately 50 nm and the length of the needle-like phase was approximately 100–200 nm. For the as-dealloyed $Al_{81}Ag_{15}Ce_4$-573 K sample, as shown in Fig. 2a, its surface exhibited an open, particle-channel structure, and the corresponding cross-section image showed a similar morphology (Fig. 2b). When the Ce content in the precursory alloy increased to 6% ($Al_{79}Ag_{15}Ce_6$), as shown in Fig. 2c and d, the needle-like morphology became clearer, and the fraction of the phase increased drastically, while the larger nanoparticles could still be observed. For the dealloyed $Al_{84}Ag_{10}Ce_6$ ribbons-573 K, the surface was similar, but the width of the needle-like phase increased and a few large particles could be observed, especially in the cross-view, as shown in Fig. 2d. The insets of Fig. 2b, d and f show the section-view of low-magnification SEM images. It can be seen that sections of the monolithic samples have been dealloyed through whole ribbons, and the average ribbon thickness is about 23.0 (±3.0) μm. Therefore, the structure of the dealloyed Al–Ag–Ce ribbons-573 K is a 3D Ag/CeO_2 architecture.

TEM and HRTEM images of the Ag/CeO_2 architecture are presented in Fig. 3. The dealloyed $Al_{79}Ag_{15}Ce_6$ samples, as shown in Fig. 3a, consisted of larger particles with a size of 20–70 nm and nanorods with the width of 7–16 nm. After the samples were calcined, some small nanoparticles could be observed on the surfaces of the nanorods (Fig. 3b) and the corresponding selected area electron diffraction (SAED) pattern is presented in Fig. 3c. And the diffraction ring patterns were identified as $Ag_{(111)}$ and the (111), (200) and (311) reflections of CeO_2. The high magnification TEM image in Fig. 3d shows that the Ag/CeO_2 architecture from the dealloyed $Al_{79}Ag_{15}Ce_6$-573 K clearly contained many ultra-small nanoparticles that were highly dispersed and loaded on the surfaces of the CeO_2 nanorods. As shown in Fig. 3e, a typical HRTEM image focusing on a specific part of an individual nanorod (circled area, Fig. 3d), reveals that the *d*-spacings were 0.24 and 0.31 nm, corresponding to the (111) plane of Ag and (111) plane of CeO_2, respectively. According to these results, it can be concluded that the larger particles were fcc-Ag while the needle-like phase was CeO_2 nanorods.

The ultra-small spherical Ag nanoparticles with a diameter of approximately 8 nm were found to be anchored and uniformly distributed on the surface of the CeO_2 nanorods with a width of 18 nm. And the interface was created in the Ag/CeO_2 nanorod architecture from the dealloyed $Al_{79}Ag_{15}Ce_6$ ribbons-573 K. The Ag particle size distribution histograms have been given in Fig. S2.† The result showed that the Ag nanoparticles in the dealloyed $Al_{79}Ag_{15}Ce_6$ ribbons-573 K exhibited a bimodal size distribution: one was around 5.91 nm, and the other was centered at 37.80 nm. When the Ag content decreased to 10 at% in the precursor alloys, the number of larger particles obviously decreased while the CeO_2 nanorods dramatically increased. The TEM/HRTEM observation confirmed that the small nanoparticles supported on the CeO_2 nanorods were indeed ultra-

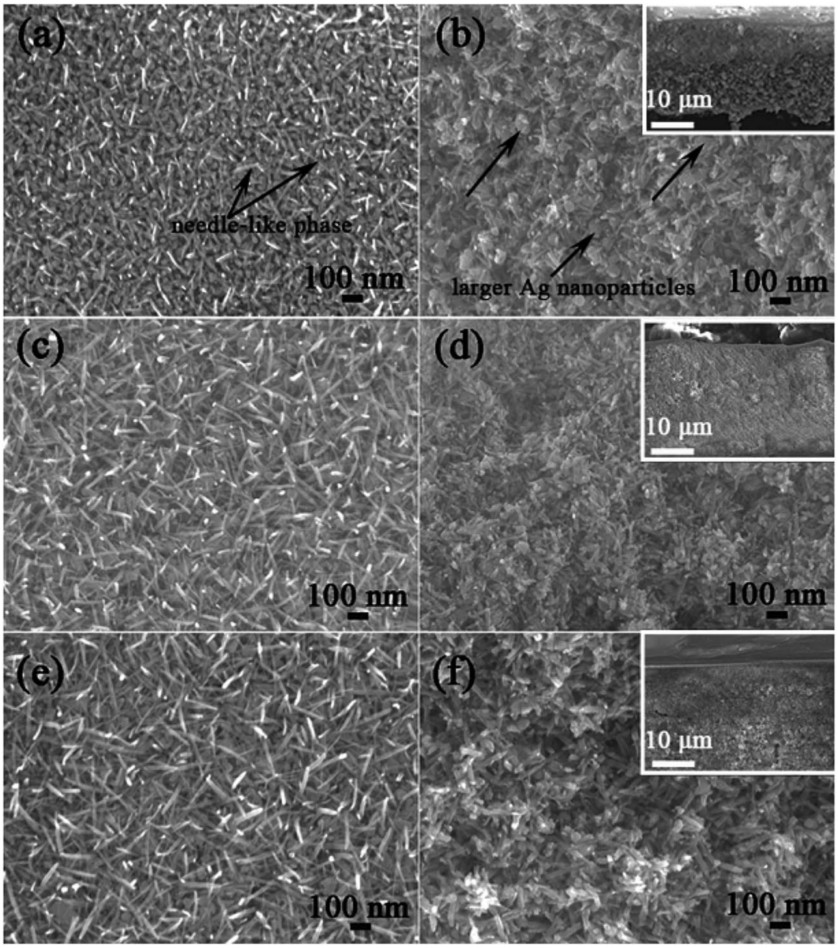

Fig. 2 Plan-view SEM images of the dealloyed $Al_{81}Ag_{15}Ce_4$ (a), $Al_{79}Ag_{15}Ce_6$ (c) and $Al_{84}Ag_{10}Ce_6$ (e) ribbons calcined at 573 K. (b), (d) and (f) showing the corresponding section-view. Insets are low magnification section-view images with the substrate.

small Ag nanoparticles. The TEM image of a CeO_2 sample (Fig. 3g) also displayed a nanorod structure, and the *d*-space of the HRTEM image confirmed that the nanorods were CeO_2 (Fig. 3h). For comparison, the TEM image of Ag was also shown in Fig. 3i and it exhibited a typical nanoporous structure. The aforementioned results demonstrate that the structure of the 3D Ag/CeO_2 nanorod architecture was constructed from the CeO_2 nanorods, the uniformly distributed large-sized Ag nanoparticles, and the ultra-small Ag nanoparticles that were anchored on the CeO_2 nanorods.

N_2 adsorption–desorption isotherms and pore size distributions of the Ag/CeO_2 nanorod architecture are shown in Fig. 4. All the isotherms were of type IV and exhibited H3 hysteretic loops of the mesoporous structure, which may be a result of nanorod stacking.[32] The BET specific surface areas and other physicochemical parameters of Ag/CeO_2 and nanoporous Ag are listed in Table 1. It is evident that the specific surface area increased along with the Ce content of the precursor alloys, resulting from a rapid increase in the amount of CeO_2 nanorods. Meanwhile, the BET surface areas of the Ag/CeO_2 sample prepared from the $Al_{79}Ag_{15}Ce_6$ ribbons-573 K could reach up to 35 $m^2\ g^{-1}$, which was much larger than that of the nanoporous Ag (8 $m^2\ g^{-1}$). In addition, it had the smallest calculated pore size, narrowest pore size distribution, and largest pore volume. These results indicated that the Ce content in the precursor alloys plays multiple important roles in determining the surface properties of the Ag/CeO_2 nanorod architecture.

XPS spectra of Ce 3d and O 1s peaks of the Ag/CeO_2 nanorod architecture are shown in Fig. 5. The spectra of Ce 3d exhibited multiple peaks and could be fitted with ten components with the assignments defined in Fig. 5a. The peaks labeled u and v, u″ and v″, u‴ and v‴ were characteristics of Ce^{4+}, while the other two double labeled u^0 and v^0 and v′ and u′ were related to Ce^{3+}.[33,34] The Ce 3d spectrum was a mixture of both Ce^{3+} and Ce^{4+} oxidation state. The concentration of Ce^{3+} was reflected by the integrated areas of the corresponding peaks, which increased with increasing Ce content in the precursor alloys. The surface Ce^{3+} concentrations of total Ce on the Ag/CeO_2 nanorod architecture obtained from different Al–Ag–Ce alloys were 15.91%, 20.98% and 23.89%, respectively (Table 1). The broad O 1s peak (Fig. 5b) at about 529, 532 and 533 eV for Ag/CeO_2 were assigned to lattice oxygen (O_{lat}), surface adsorbed oxygen (O_{sur}) and weakly bonded oxygen species (O_{bon}), respectively.[20,34] The highly mobile O_{sur} oxygen species is generally more important for oxidation reactions compared to

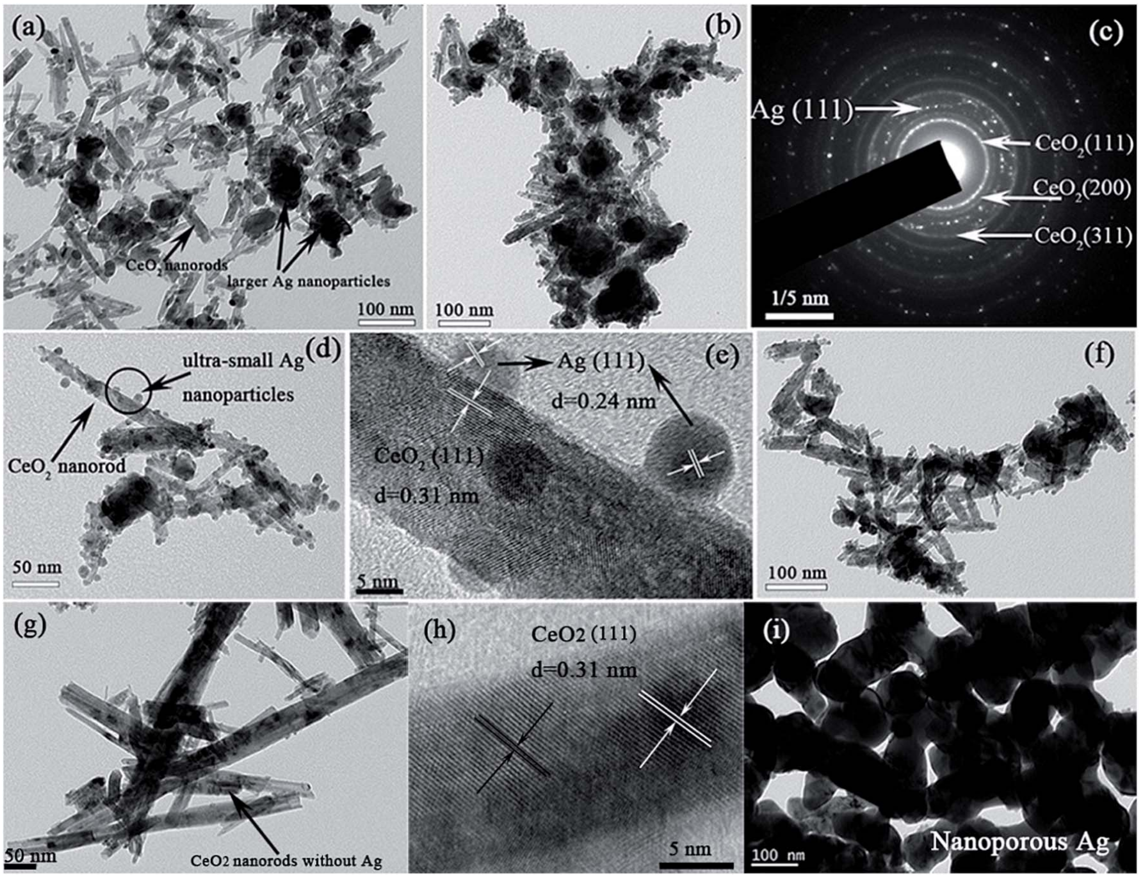

Fig. 3 TEM images of the Ag/CeO$_2$ nanorod architecture prepared from the dealloyed $Al_{79}Ag_{15}Ce_6$ ribbons (a), the dealloyed sample (b and d) and the dealloyed $Al_{84}Ag_{10}Ce_6$ sample (f) calcined at 573 K. SAED patterns (c) corresponding to (b) and an HRTEM image (e) of the dealloyed $Al_{79}Ag_{15}Ce_6$ ribbon-573 K. TEM (g) and HRTEM (h) images of CeO$_2$ without Ag prepared from dealloyed $Al_{90}Ce_{10}$ ribbon-573 K. A TEM images (i) of nanoporous Ag from the dealloyed $Al_{81}Ag_{15}$ ribbon.

the O_{lat} and O_{bon} species.[35,36] The relative concentration ratios of $O_{sur}/(O_{lat} + O_{sur} + O_{bon})$ for each sample are estimated from the areas of the O_{lat}, O_{sur} and O_{bon} peaks (Table 1). The highest relative content of O_{sur} was obtained on the surface of the Ag/CeO$_2$ sample from the dealloyed $Al_{79}Ag_{15}Ce_6$ alloy (42.20%). The results indicate that the ratio of Ag/Ce in the precursor alloys has a significant influence on the concentration of Ce^{3+} and the active surface oxygen species.

Fig. S3† shows the Ag 3d XPS spectra of Ag/CeO$_2$ nanorods and nanoporous Ag. For the dealloyed $Al_{85}Ag_{15}$ ribbons, the two

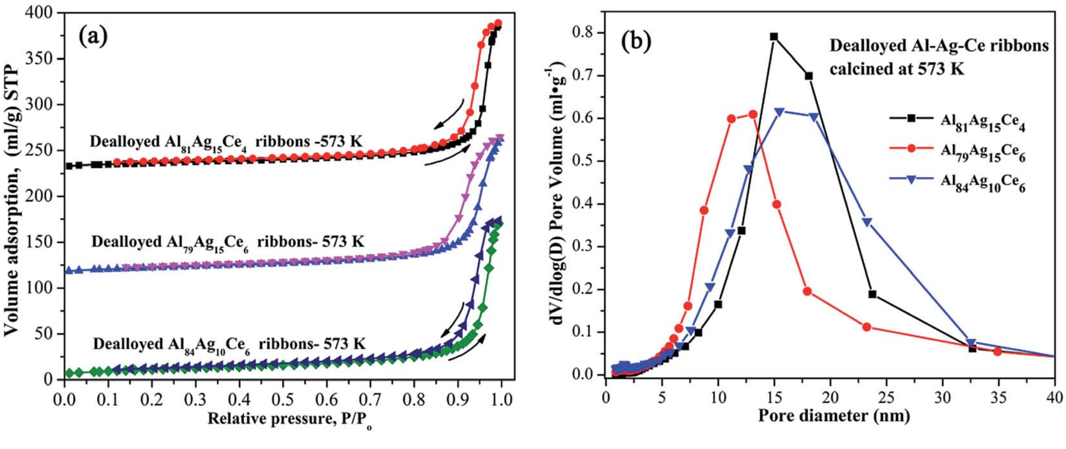

Fig. 4 Nitrogen adsorption–desorption isotherms (a) and corresponding pore size distributions (b) of dealloyed $Al_{81}Ag_{15}Ce_4$, $Al_{79}Ag_{15}Ce_6$ and $Al_{84}Ag_{10}Ce_6$ ribbons calcined at 573 K.

Table 1 BET surface area (S_{BET}), average pore diameter (D_P), pore volume (V_P), the relative quantity of surface adsorbed oxygen species [$O_{sur}/(O_{lat} + O_{sur} + O_{bon})$%] and Ce^{3+} ions [$Ce^{3+}/(Ce^{3+} + Ce^{4+})$%] of the dealloyed $Al_{81}Ag_{15}Ce_4$, $Al_{79}Ag_{15}Ce_6$ and $Al_{84}Ag_{10}Ce_6$ ribbons calcined at 573 K and the dealloyed $Al_{85}Ag_{15}$ ribbons

Samples	S_{BET} ($m^2\ g^{-1}$)	D_P (nm)	V_P ($cm^3\ g^{-1}$)	$O_{sur}/(O_{lat} + O_{sur} + O_{bon})$%	$Ce^{3+}/(Ce^{3+} + Ce^{4+})$%
$Al_{81}Ag_{15}Ce_4$	29	13	0.1779	40.54	15.91
$Al_{79}Ag_{15}Ce_6$	35	10	0.1990	42.20	20.98
$Al_{84}Ag_{10}Ce_6$	37	11	0.1879	39.08	23.89
$Al_{85}Ag_{15}$	8	13	0.0283	N.A	N.A

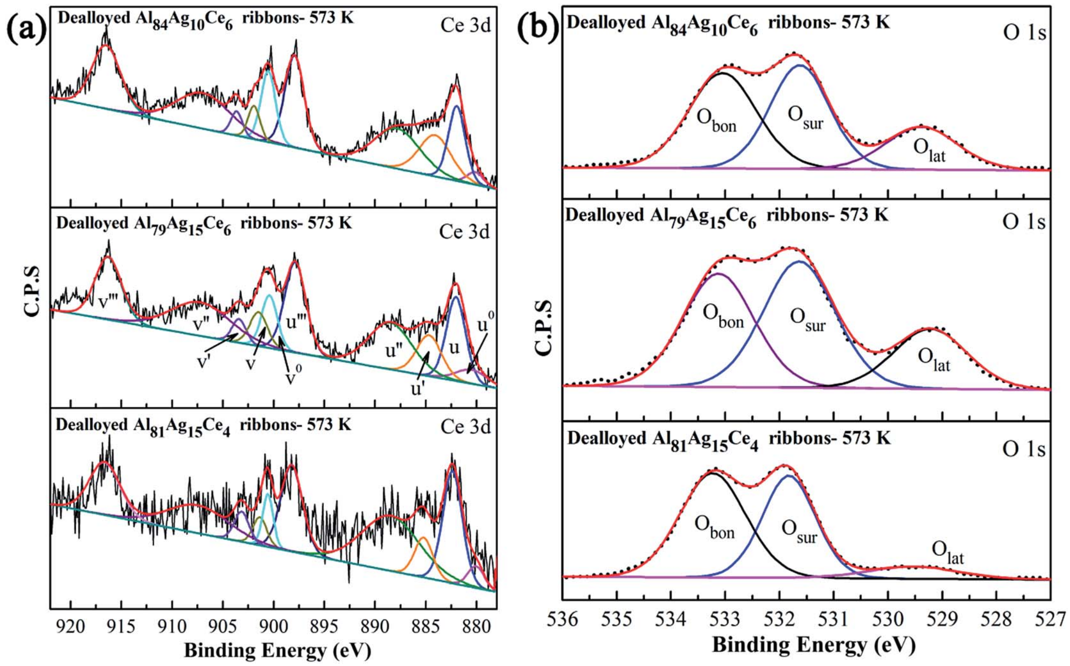

Fig. 5 XPS spectra of Ce 3d (a) and O 1s (b) of the Ag/CeO_2 nanorod architecture prepared from the dealloyed Al–Ag–Ce ribbons calcined at 573 K.

peaks of Ag $3d_{5/2}$ and Ag $3d_{3/2}$ at 368.2 and 374.2 eV could be assigned to metallic silver. After the addition of Ce into the Al–Ag alloy, the binding energy of the Ag/CeO_2 nanorods slightly shifted to a lower value of 368.0 eV, indicating the occurrence of a partial charge transfer between Ag and CeO_2,[23] as well as the formation of an oxidation state for Ag nanoparticles anchored on the surface of the composite.[25]

The dealloying of the melt-spun Al–Ag–Ce ribbons combined with calcination led to the formation of bimodal Ag nanoparticles supported on the 3D CeO_2 nanorod architecture. The formation mechanism can be depicted as follows. As the removal of Al from alloys in the NaOH aqueous solution, the Ag and Ce atoms are released and form a mixture of Ag and Ce. Some fast diffused Ag adatoms are hindered by Ce and gradually accumulate, resulting in the formation of Ag nanoparticles with a size of 20–70 nm. Ce atoms at the surface of the Ce-rich Ag–Ce mixture can quickly react with hot water to generate nuclei of cerium hydroxide. The formation process of CeO_2 nanorod has been discussed in our previous work.[37] During the formation of CeO_2, nanorods from different nuclei bond with each other to form the 3D architecture. These processes mainly occur on the surface scale of the Ag–Ce mixture with an outer layer of Ce oxide, and only the CeO_2 surface scale is formed. Some Ag atoms are also enriched in the mixture. When undergoing further oxidation, especially calcination, the Ce atoms would diffuse from the Ag–Ce mixture toward the mixture-oxide interface, while Ag diffuses in the opposite direction according to published reports.[38–40] The mixture–oxide interface is stable until the Ce is completely oxidized to CeO_2, thus forming a highly rugged alloy–oxide interface.[38–40] As a consequence, the aggregated Ag atoms or clusters in other sides formed Ag nanoparticles on the surface of the CeO_2 nanorods, where they are partly embedded and immobilized. After the Al–Ag alloys were dealloyed, nanoporous Ag exhibited an interpenetrating porous structure with some bicontinuous Ag ligaments (Fig. 3i). When 6 at% Ce was added into the Al–Ag alloy and dealloyed, bicontinuous Ag ligaments became small isolated Ag particles and they did not form bicontinuous Ag ligaments (Fig. 3a). After calcination, CeO_2 nanorod-based frameworks build the 3D architecture while small isolated Ag particles grew and aggregated to form larger particles, which then serve as the current collector for transferring the generated electrons at the contacted interface. The calcination process essentially promotes a close contact between the Ag nanoparticles and the CeO_2 nanorods.

3.2 Electrocatalytic oxidation of sodium borohydride on Ag/CeO_2 electrodes

In order to optimize the heat treatment temperature of the prepared composites, the dealloyed $Al_{79}Ag_{15}Ce_6$ ribbons were calcined at between 373 and 673 K. Fig. S4† shows the CV curves of BH_4^- oxidation on the Ag/CeO_2 electrodes. According to the literature,[41,42] the oxidation peaks at around −0.3 V in the CV curves of the prepared electrodes corresponded to the direct oxidation of BH_4^-. The current density peaks of all the calcined Ag/CeO_2 ribbons for BH_4^- oxidation obviously increased with increased calcination temperatures up to 573 K. When the temperature further increased to 673 K, the oxidation peak showed a slight decrease, which may result from growth of Ag nanoparticles and the slight coarsened structure of Ag/CeO_2 composite. These results indicated that the calcination temperature had an effect on the catalytic activities toward the $NaBH_4$ oxidation and the optimized treatment temperature is 573 K in the investigated temperatures.

Catalytic activity is closely related to the structure and surface composition of the electrode. Fig. 6 shows the cyclic voltammetry recorded for the Ag/CeO_2 nanorod and Ag electrodes with 0.01 M $NaBH_4$ + 0.5 M KOH solution at a scan rate of 100 mV s^{-1}. The current densities of the CV plots in Fig. 6a and b were calculated using surface specific current and mass specific current, respectively. The current densities of the anode peaks for BH_4^- oxidation on Ag and that of Ag/CeO_2 from $Al_{81}Ag_{15}Ce_4$, $Al_{79}Ag_{15}Ce_6$ and $Al_{84}Ag_{10}Ce_6$ electrodes were 16.89, 26.61, 25.65 and 16.24 mA cm^{-2}, respectively (Fig. 6a). Furthermore, an accurate estimation of the intrinsic electrocatalytic activities of the catalysts could be made if the current density is calculated from the unit mass of Ag (as estimated in Table S2†). The current densities of the CV curves in Fig. 6b were calculated based on the Ag mass. The highest specific mass current density of the oxidation peak, 2.97 mA mg^{-1}, was obtained from an Ag/CeO_2 electrode prepared from the $Al_{79}Ag_{15}Ce_6$ alloy-573 K, which was about 2.5 times higher than that from the nanoporous Ag electrode prepared from $Al_{85}Ag_{15}$ under the same conditions. These results reveal that the introduction of low-cost CeO_2 not only effectively reduces the required amount of Ag, but also results in an initial increase of catalytic activity for BH_4^- oxidation in comparison with pure Ag counterparts.

Fig. 7a shows the effect of scan rate on the current densities of the Ag/CeO_2 electrodes obtained from the $Al_{79}Ag_{15}Ce_6$ alloy-573 K for $NaBH_4$ electrooxidation in 0.01 M $NaBH_4$ + 0.5 M KOH. The peak current density increased and shifted to more positive potentials with increasing scan rate and no corresponding reduction peak occurred in the negative scan, which demonstrates that the electrochemical reaction of $NaBH_4$ was irreversible.[31,42] The peak current density varied linearly with the square root of the scan rate, as shown in Fig. 7b, which proved that the electrochemical reaction process was controlled by diffusion and mass transport[43] within the investigated scan rates range on the Ag/CeO_2 electrodes.

Fig. 8 shows the chronoamperometric response of Ag and Ag/CeO_2 electrodes in 0.01 M $NaBH_4$ + 0.5 M KOH solution. The current density of the catalysts electrodes declined over time during BH_4^- electrooxidation. After approximately 75 s, the current density became stable and only slightly declined. The current density stabilized at approximately 2.67, 2.42, 1.49 and 2.21 mA cm^{-2} for the Ag/CeO_2 and Ag electrodes, respectively, after reaction for 480 s. The Ag/CeO_2 catalysts prepared from the $Al_{79}Ag_{15}Ce_6$ and $Al_{81}Ag_{14}Ce_4$ ribbons-573 K exhibited higher catalytic activity for BH_4^- electrooxidation than Ag catalysts without CeO_2, which was consistent with the CV measurements.

It is very important for an electrocatalyst to maintain increased stability against degradation. Electrocatalytic stability of the Ag/CeO_2 electrode was studied by numerous cycling in a 0.01 M $NaBH_4$ + 0.5 M KOH solution between −1.0 and 0.6 V.

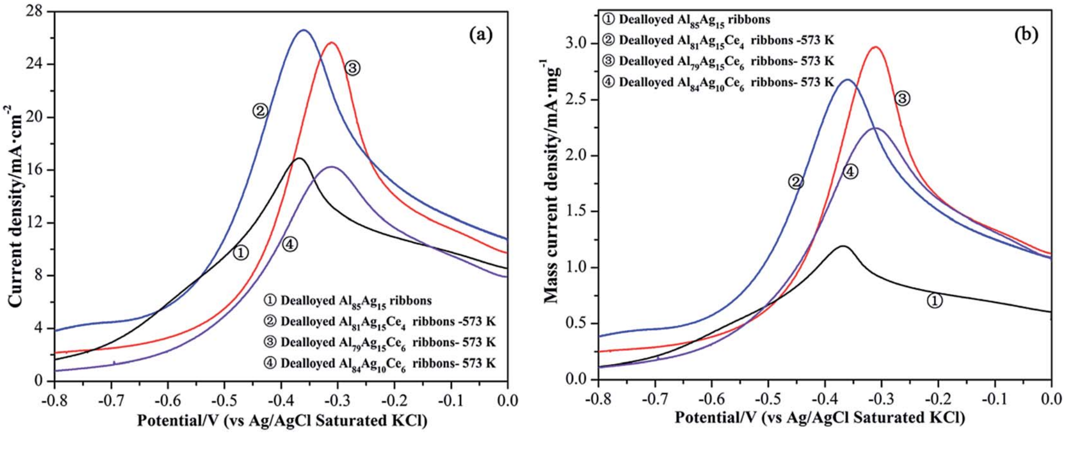

Fig. 6 CV curves of BH_4^- oxidation on the Ag/CeO_2 nanorods and Ag electrodes in 0.01 M $NaBH_4$ + 0.5 M KOH at a scan rate of 100 mV s^{-1}. Ag/CeO_2 was prepared through the dealloyed Al–Ag–Ce alloys calcined at 573 K. Current density was given on the basis of surface specific current (a) and mass specific current (b).

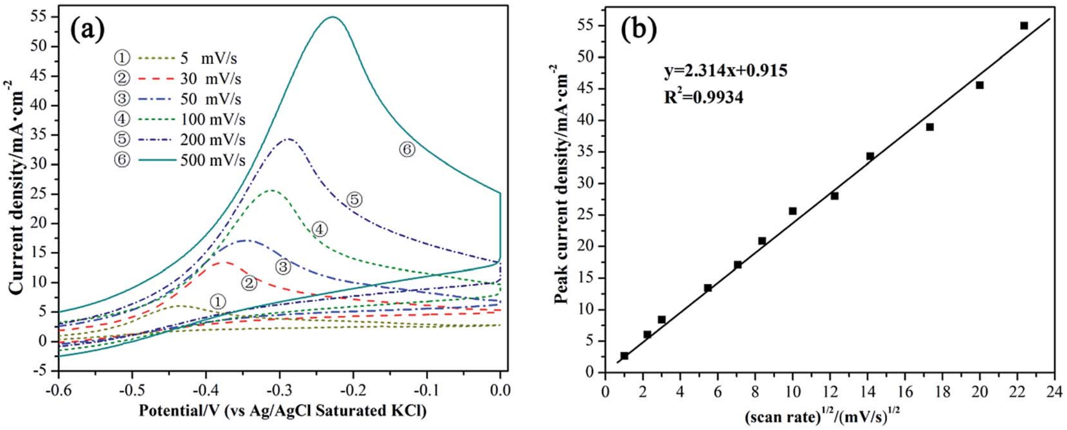

Fig. 7 CV curves of 0.01 M $NaBH_4$ in a 0.5 M KOH solution on the Ag/CeO_2 nanorod electrodes at different scan rates (a) and variation plot of the peak current density *vs.* the square root of the voltage scan rate (b). The electrode was prepared from the dealloyed $Al_{79}Ag_{15}Ce_6$ ribbons calcined at 573 K.

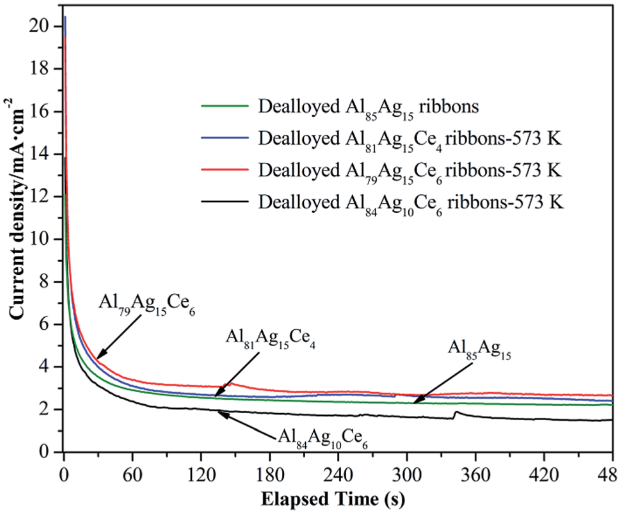

Fig. 8 CA curves (at −0.4 V *vs.* Ag/AgCl, KCl) for Ag/CeO_2 nanorods and Ag electrode in 0.01 M $NaBH_4$ + 0.5 M KOH.

Fig. 9 shows a set of continuous CVs up to 81 scanning cycles for the Ag/CeO_2 electrode at 20 mV s^{-1}. It can be seen that the peak current density on the prepared electrode at around −0.4 V decreased with potential cycling with respect to the BH_4^- oxidation reaction. This indicated that the catalyst was not sufficiently stable during long-term cycling. Degradation of the catalyst may be related to the fast decay of electrochemical reaction due to the low concentration of $NaBH_4$,[44] which is similar to the reported nano-Au(Co)/Ti and graphene–cobalt–nickel nano-ensemble electrocatalysts.[44,45]

EIS can be used to determine the charge transfer resistance of the electrode surface during an electrochemical reaction. Fig. 10 shows the impedance plots of the Ag and Ag/CeO_2 electrodes. The spectra display a semicircle in the high frequency region owing to the electron transfer limited process, while the straight line in the low frequency region can be attributed to the diffusion process.[46] The electron transfer resistance (R_{ct}) at the electrode surface is proportional to the semicircle diameter of the Nyquist plots. Compared with the Ag electrodes, the diameters of the Nyquist circle for Ag/CeO_2 obtained from $Al_{81}Ag_{15}Ce_4$ and $Al_{79}Ag_{15}Ce_6$ alloys showed only a slight increase, revealing that the ability for charge transfer at the Ag/CeO_2 electrode surface was similar to that at the Ag electrode surface. Although the Ag content and conductivity of the Ag/CeO_2 electrodes were less than those of pure Ag, the R_{ct}s of Ag/CeO_2 did not increase. This could be attributed to the electronic inductive effect of the interfacial interaction. With further increases in the Ce content, the diameter of the semicircle visibly increased, indicating that the excess CeO_2 blocked electron transfer from the electrolyte to the electrode surface.

Our results show that the catalytic activity of the Ag/CeO_2 nanorod electrodes was higher than that of the pure Ag electrodes and that the mass current density of the Ag/CeO_2 catalyst was about 2.5 times as high as that of pure Ag. The relatively

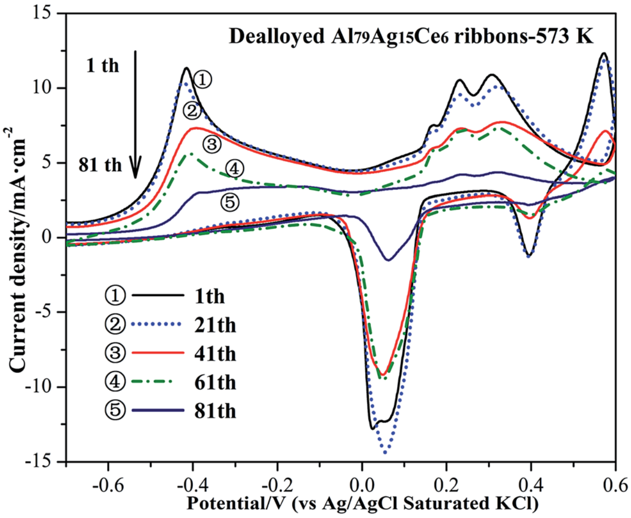

Fig. 9 Long-term CVs of Ag/CeO_2 catalyst recorded in 0.01 M $NaBH_4$ + 0.5 M KOH at 20 mV s^{-1}. The catalyst was prepared from the dealloyed $Al_{79}Ag_{15}Ce_6$ ribbons calcined at 573 K.

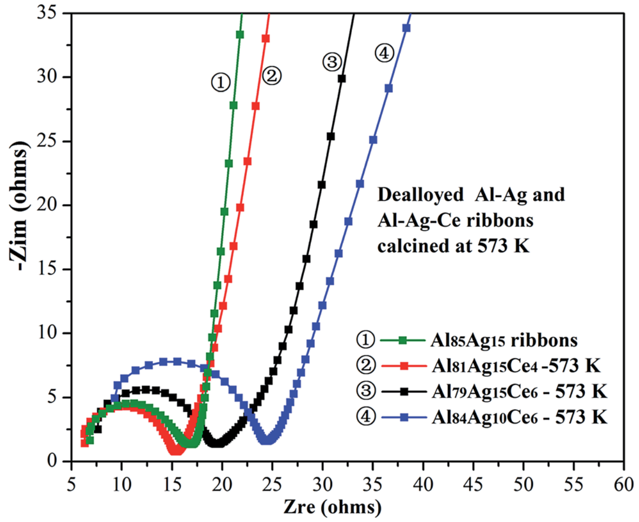

Fig. 10 Nyquist diagrams of the Ag and Ag/CeO$_2$ electrodes in 0.01 M NaBH$_4$ + 0.5 M KOH.

high electrocatalytic activity of the Ag/CeO$_2$ with different Ag/Ce ratios can be attributed to the high concentration oxygen vacancies and the strong interfacial interaction between ultra-small Ag nanoparticles and the CeO$_2$ nanorods that resulted from the unique structure.

It has been demonstrated that Ag and Ag-based nanocomposites are excellent catalytic materials as anode materials for BOR and the reaction on the Ag electrodes mainly occur on the Ag$_2$O surface.[29,41,47,48] The surface oxidation of Ag electrodes has a considerable catalytic effect on the BOR for Ag-based catalysts.[14,15] Shimizu *et al.* have reported that the active oxygen species on the Ag–Ce catalyst has a similar activity to that of the lattice oxygen of Ag$_2$O.[49] On one hand, the XPS results suggested that the Ce^{3+} concentration on the surface of the samples increased with increasing Ce content in the precursor alloys and evidenced a corresponding high amount of oxygen vacancies, which can significantly improve intrinsic electrocatalytic activity (Fig. 6b). The oxygen vacancies absorb oxygen species (*i.e.*, OH$_{ads}$) and can generate adsorbed atomic oxygen and hydroxyls, which greatly influences the redox properties of the supported metal-species.[50] The abundant oxygen vacancies provide absorption sites for surface oxygen species to form and transform the active oxygen and electron, which are transferred to Ag nanoparticles through their interface.[29,51,52] On the other hand, a robust interaction exists between CeO$_2$ nanorods and the Ag nanoparticles, which can greatly enhance their electrocatalytic performance for BH$_4^-$ oxidation. After adding Ce to the precursor alloy, the XPS peaks of Ag 3d displayed a slightly negative shift to lower values due to the electron transfer (Fig. S3†). The occurrence of electron transfer between Ag and CeO$_2$, associated with strengthened interfacial interactions, was responsible for facilitating the uptake of electrons by reactant molecules, as reported elsewhere for Ag@CeO$_2$ catalyst.[23,53] According to Luches *et al.*,[15] the increase in Ce^{3+} concentration along with the amount of small Ag nanoparticles deposited also supported the postulate that part of CeO$_2$ is reduced by electron transfer. These evidence indicated that the addition of Ce to the precursor alloy modifies the electronic structure of Ag and produces an electronic interaction between Ag and CeO$_2$. In addition, the lower binding energy can decrease the chemisorption ability of the adsorbate, and allow the efficient removal of the adsorbed reaction intermediate during electrochemical reactions, thus resulting in an improvement of activity. Therefore, the enhanced catalytic activity for BOR should be attributed to the high fraction of the active oxygen species and the strengthened interactions between Ag and CeO$_2$.

The unique 3D Ag/CeO$_2$ nanorod architecture provides a high specific surface area and improved access to the Ag species. Firstly, CeO$_2$ nanorods and Ag particles produce interconnected porous channels that could provide a larger reaction space for catalytic reactions, which can effectively facilitate conductive ion transfer and reactant molecules transport for the electrocatalysis.[31,54] A suitable amount of CeO$_2$ in the Ag/CeO$_2$ samples not only decreased the pore size but also narrowed the pore size distribution (Fig. 4), leading to higher catalytic activity (Fig. 6) and electrochemical stability (Fig. 8) of the Ag/CeO$_2$ electrode. Secondly, highly conductive Ag particles can serve as a bridge to promote the transfer of electrons. After calcination, the *in situ* growth of ultra-small Ag nanoparticles supported on the CeO$_2$ nanorods facilitated the formation of well-defined interfaces, and provided a high interfacial area. These resulted in enhanced interfacial interaction between Ag and CeO$_2$, effectively reducing any additional contact resistance. EIS results suggested that the reinforced interfacial electronic interaction between Ag and CeO$_2$ can overcome the adverse impact of low electron conductivity of CeO$_2$ nanorods.[17,29] Such a unique structure can provide more active sites and efficiently improve the electrochemical performance toward BH$_4^-$ oxidation.

4. Conclusions

A 3D Ag/CeO$_2$ nanorod architecture was prepared by a facile dealloying method, and bimodal Ag nanoparticles supported on the 3D CeO$_2$ nanorod architecture formed after calcination. Ag nanoparticles with an average size of approximately 8 nm were loaded on the CeO$_2$ nanorod framework, generating nanoscale interfaces. The highly conductive large-sized Ag particles with diameter of 20–70 nm connected the nanostructures as bridges for electron transport. This novel structure can fully utilize Ag to improve the conductivity of the synthesized composites for electrocatalysis. The interfaces between the Ag nanoparticles and the CeO$_2$ nanorods can promote the generation of oxygen vacancies and active oxygen species. The 3D Ag/CeO$_2$ architecture exhibits enhanced catalytic activity for BH$_4^-$ oxidation, which can be attributed to the unique structures and the nanoscale Ag/CeO$_2$ interfacial interaction. This work provides a simple strategy for the fabrication of 3D rare earth oxide/noble metal nanostructures to amplify noble metal/oxide interactions.

Acknowledgements

This work was supported by the National Natural Science Foundation of China (Grant No. 51371135).

References

1 E. Gyenge, *Electrochim. Acta*, 2004, **49**, 965–978.

2 K. Cheng, D. Cao, F. Yang, D. Zhang, P. Yan, J. Yin and G. Wang, *J. Power Sources*, 2013, **242**, 141–147.

3 P.-Y. Olu, A. Bonnefont, M. Rouhet, S. Bozdech, N. Job, M. Chatenet and E. Savinova, *Electrochim. Acta*, 2015, **179**, 637–646.

4 R. Valiollahi, R. Ojani and J.-B. Raoof, *Electrochim. Acta*, 2016, **191**, 230–236.

5 I. Merino-Jimenez, M. Janik, C. P. de Leon and F. Walsh, *J. Power Sources*, 2014, **269**, 498–508.

6 P.-Y. Olu, B. Gilles, N. Job and M. Chatenet, *Electrochem. Commun.*, 2014, **43**, 47–50.

7 H.-J. Qiu, X. Shen, J. Wang, A. Hirata, T. Fujita, Y. Wang and M. Chen, *ACS Catal.*, 2015, **5**, 3779–3785.

8 X. Wang, D. Liu, S. Song and H. Zhang, *J. Am. Chem. Soc.*, 2013, **135**, 15864–15872.

9 G. Xi, J. Ye, Q. Ma, N. Su, H. Bai and C. Wang, *J. Am. Chem. Soc.*, 2012, **134**, 6508–6511.

10 B. Wu and N. Zheng, *Nano Today*, 2013, **8**, 168–197.

11 H.-P. Zhou, H.-S. Wu, J. Shen, A.-X. Yin, L.-D. Sun and C.-H. Yan, *J. Am. Chem. Soc.*, 2010, **132**, 4998–4999.

12 S. Hosokawa, M. Taniguchi, K. Utani, H. Kanai and S. Imamura, *Appl. Catal., A*, 2005, **289**, 115–120.

13 D. Valechha, S. Lokhande, M. Klementova, J. Subrt, S. Rayalu and N. Labhsetwar, *J. Mater. Chem.*, 2011, **21**, 3718–3725.

14 Y. Zhou, Y. Gao, Y. Liu and J. Liu, *J. Power Sources*, 2010, **195**, 1605–1609.

15 P. Luches, F. Pagliuca, S. Valeri, F. Illas, G. Preda and G. Pacchioni, *J. Phys. Chem. C*, 2011, **116**, 1122–1132.

16 A. Younis, D. Chu and S. Li, *J. Mater. Chem. A*, 2015, **3**, 13970–13977.

17 Y. Y. Chu, Z. B. Wang, Z. Z. Jiang, D. M. Gu and G. P. Yin, *Adv. Mater.*, 2011, **23**, 3100–3104.

18 M. A. Scibioh, S.-K. Kim, E. A. Cho, T.-H. Lim, S.-A. Hong and H. Y. Ha, *Appl. Catal., B*, 2008, **84**, 773–782.

19 A. Gomathi, S. M. Vickers, R. Gholami, M. Alyani, R. W. Man, M. J. MacLachlan, K. J. Smith and M. O. Wolf, *ACS Appl. Mater. Interfaces*, 2015, **7**, 19268–19273.

20 E. Varga, P. Pusztai, A. Oszkó, K. Baan, A. Erdőhelyi, Z. Kónya and J. Kiss, *Langmuir*, 2016, **32**, 2761–2770.

21 D. Duan, H. Liu, X. You, H. Wei and S. Liu, *J. Power Sources*, 2015, **293**, 292–300.

22 T. Mitsudome, Y. Mikami, M. Matoba, T. Mizugaki, K. Jitsukawa and K. Kaneda, *Angew. Chem., Int. Ed.*, 2012, **51**, 136–139.

23 J. Zhang, L. Li, X. Huang and G. Li, *J. Mater. Chem.*, 2012, **22**, 10480–10487.

24 S. Chang, M. Li, Q. Hua, L. Zhang, Y. Ma, B. Ye and W. Huang, *J. Catal.*, 2012, **293**, 195–204.

25 L. Ma, D. Wang, J. Li, B. Bai, L. Fu and Y. Li, *Appl. Catal., B*, 2014, **148**, 36–43.

26 H. Chen, J. Duan, X. Zhang, Y. Zhang, C. Guo, L. Nie and X. Liu, *Mater. Lett.*, 2014, **126**, 9–12.

27 Z. Zhang, Y. Wang, Z. Qi, W. Zhang, J. Qin and J. Frenzel, *J. Phys. Chem. C*, 2009, **113**, 12629–12636.

28 C. Xu, R. Wang, M. Chen, Y. Zhang and Y. Ding, *Phys. Chem. Chem. Phys.*, 2010, **12**, 239–246.

29 G. Li, F. Lu, X. Wei, X. Song, Z. Sun, Z. Yang and S. Yang, *J. Mater. Chem. A*, 2013, **1**, 4974–4981.

30 A. Manshina, A. Povolotskiy, A. Povolotckaia, A. Kireev, Y. Petrov and S. Tunik, *Appl. Surf. Sci.*, 2015, **353**, 11–16.

31 X. Zhang, C. Wei, Y. Song, X. Song and Z. Sun, *Int. J. Hydrogen Energy*, 2014, **39**, 15646–15655.

32 L. Wang, J. Ding, Y. Chai, Q. Liu, J. Ren, X. Liu and W.-L. Dai, *Dalton Trans.*, 2015, **44**, 11223–11234.

33 X. Yao, Y. Xiong, W. Zou, L. Zhang, S. Wu, X. Dong, F. Gao, Y. Deng, C. Tang and Z. Chen, *Appl. Catal., B*, 2014, **144**, 152–165.

34 D. Devaiah, T. Tsuzuki, T. Boningari, P. G. Smirniotis and B. M. Reddy, *RSC Adv.*, 2015, **5**, 30275–30285.

35 Y. R. Zheng, M. R. Gao, Q. Gao, H. H. Li, J. Xu, Z. Y. Wu and S. H. Yu, *Small*, 2015, **11**, 182–188.

36 S. Cai, D. Zhang, L. Zhang, L. Huang, H. Li, R. Gao, L. Shi and J. Zhang, *Catal. Sci. Technol.*, 2014, **4**, 93–101.

37 X. Zhang, K. Li, W. Shi, C. Wei, X. Song, S. Yang and Z. Sun, *Nanotechnology*, 2016, **28**, 045602.

38 C. Wagner, *J. Electrochem. Soc.*, 1956, **103**, 571–580.

39 C. Wagner, *J. Electrochem. Soc.*, 1952, **99**, 369–380.

40 B. D. Lichter and C. Wagner, *J. Electrochem. Soc.*, 1960, **107**, 168–180.

41 E. Sanlı, H. Çelikkan, B. Z. Uysal and M. L. Aksu, *Int. J. Hydrogen Energy*, 2006, **31**, 1920–1924.

42 H. Çelikkan, M. Şahin, M. L. Aksu and T. N. Veziroğlu, *Int. J. Hydrogen Energy*, 2007, **32**, 588–593.

43 M. S. Ahmed, D. Park and S. Jeon, *J. Power Sources*, 2016, **308**, 180–188.

44 S. Saha, S. Ganguly, D. Banerjee and K. Kargupta, *Int. J. Hydrogen Energy*, 2015, **40**, 1760–1773.

45 L. Tamašauskaitė-Tamašiūnaitė, A. Jagminienė, A. Balčiūnaitė, A. Zabielaitė, A. Žielienė, L. Naruškevičius, J. Vaičiūnienė, A. Selskis, R. Juškėnas and E. Norkus, *Int. J. Hydrogen Energy*, 2013, **38**, 14232–14241.

46 X. Kang, J. Wang, H. Wu, I. A. Aksay, J. Liu and Y. Lin, *Biosens. Bioelectron.*, 2009, **25**, 901–905.

47 E. Sanli, B. Z. Uysal and M. L. Aksu, *Int. J. Hydrogen Energy*, 2008, **33**, 2097–2104.

48 D. Duan, Q. Wang, H. Liu, X. You, S. Liu and Y. Wang, *J. Solid State Electrochem.*, 2016, 1–13.

49 K. I. Shimizu, H. Kawachi and A. Satsuma, *Appl. Catal., B*, 2010, **96**, 169–175.

50 H. Tan, J. Wang, S. Yu and K. Zhou, *Environ. Sci. Technol.*, 2015, **49**, 8675–8682.

51 X. Liu, K. Zhou, L. Wang, B. Wang and Y. Li, *J. Am. Chem. Soc.*, 2009, **131**, 3140–3141.

52 S. Hu, Y. Wang, W. Wang, Y. Han, Q. Fan, X. Feng, Q. Xu and J. Zhu, *J. Phys. Chem. C*, 2015, **119**, 3579–3588.

53 Y.-Y. Wang, Y. Shu, J. Xu and H. Pang, *CrystEngComm*, 2017, **19**, 684–689.

54 C. Dong, H. Zhong, T. Kou, J. Frenzel, G. Eggeler and Z. Zhang, *ACS Appl. Mater. Interfaces*, 2015, **7**, 20215–20223.